Dynamic *in vivo* quantification of rod photoreceptor degeneration using fluorescent reporter mouse models of retinitis pigmentosa

Harry O. Orlans[a,b], Alun R. Barnard[a,c], Robert E. MacLaren[a,b,c]

[a]Nuffield Laboratory of Ophthalmology, Nuffield Department of Clinical Neurosciences, University of Oxford. [b]Moorfields Eye Hospital NHS Foundation Trust, London, UK. [c]Oxford Eye Hospital, Oxford, UK

Corresponding author: H. O. Orlans, Nuffield Laboratory of Ophthalmology, Department of Clinical Neurosciences & NIHR Oxford.

Email: enquiries@eye.ox.ac.uk

Declarations of interest: none

This work was supported by an MRC/Fight for Sight grant MR/N00101X/1

Abbreviations

AAV: adeno-associated virus; **AMD:** age-related macular degeneration; **ART:** automatic real time; **BAF:** blue autofluorescence; **cSLO:** confocal scanning laser ophthalmoscopy; **EGFP:** enhanced green fluorescent protein; **IRD:** inherited retinal disease; **IS:** inner segments; **mGV:** mean grey value; **NIR:** near infrared; **Nrl:** neural retina-specific leucine zipper; **OCT:** optical coherence tomography; **ONL:** outer nuclear layer; **OS:** outer segments; **PNW:** post-natal week; **qAF:** quantitative autofluorescence; **RP:** retinitis pigmentosa; **RPE:** retinal pigment epithelium; **SEM:** standard error of the mean

Abstract

Imaging techniques have revolutionised the assessment of retinal disease in humans and animal models. Here we describe a novel technique for the *in vivo* visualisation of rod photoreceptors which permits semiquantitative assessment of outer retinal degeneration, and validate this approach in two mouse models of retinitis pigmentosa (RP).

Transgenic mice carrying an *Nrl-EGFP* allele and homozygous for either knock-out of rhodopsin (*Nrl-EGFP*, $Rho^{-/-}$) or heterozygous for knock-in of P23H mutant rhodopsin (*Nrl-EGFP*, $Rho^{P23H/+}$) were used in this study. These novel strains have green fluorescent rods which undergo a progressive degeneration. Fundus imaging was performed at three-weekly intervals by near infrared reflectance (NIR) and blue light autofluorescence (BAF) confocal scanning laser ophthalmoscopy (cSLO). Mean grey values (mGV), which quantify fluorescence levels within such images, were compared for degenerate and age-matched non-degenerate (*Nrl-EGFP*, $Rho^{+/+}$) controls.

Mean grey value significantly decreased over time in the $Rho^{-/-}$ and $Rho^{P23H/+}$ groups but was maintained in $Rho^{+/+}$ mice ($P<0.001$, two-way ANOVA). This corresponded to outer nuclear layer (ONL) thinning as observed by histology. The mGV of superior retina was significantly greater than that of inferior retina in $Rho^{P23H/+}$ ($P=0.0024$) but not in age-matched $Rho^{+/+}$ ($P=0.45$) or $Rho^{-/-}$ ($P=0.65$) mice reflecting histological findings. Focal loss of rods could be visualised and mapped *in vivo* with this technique following a toxic insult, with thinning of the ONL being confirmed in hypofluorescent regions by spectral domain ocular coherence tomography (OCT).

Fluorescence labelling of rods permits *in vivo* characterisation of models of RP and may provide new insights into patterns of degeneration, or rescue effect after treatment. mGV can be used in such cases as a semiquantitative metric of ONL degeneration, and can be used to identify regional variations in photoreceptor loss.

Keywords: retina, retinitis pigmentosa, imaging, scanning laser ophthalmoscopy

1. Introduction

Retinitis pigmentosa (RP) describes a heterogeneous group of inherited retinal diseases (IRDs) characterized by progressive photoreceptor loss which results in nyctalopia, visual field constriction and in many cases, severe sight impairment. The majority of cases of RP are caused by mutations in genes essential for rod photoreceptor function and viability, and may be inherited in autosomal dominant, autosomal recessive or X-linked fashions (Hartong et al., 2006). Whilst there are at present no universally approved treatments for RP, several clinical trials encompassing gene therapy, pharmacological, and medical-device based approaches are underway, and this remains an intensive area of research worldwide (Smith et al., 2015). The pre-clinical development of new treatments for RP is heavily reliant upon the availability of suitable animal models that closely mimic the human phenotype (Rivas and Vecino, 2009). To maximise the utility of such model systems, an ability to track both spatial and temporal patterns of outer retinal degeneration with and without intervention is critical. Traditionally, anatomical changes over time and the effect on this of experimental treatments have been determined by histological means. Whilst this remains an important technique in preclinical studies, tissue sectioning for the purpose of tracking retinal degeneration has a number of notable limitations: the introduction of artefactual changes consequent upon tissue processing (McInnes, 2005); low sensitivity for detecting subtle and regional changes; an inability to visualise a single specimen in more than one plane; and the inability to measure changes longitudinally in a single animal. Moreover, deriving quantitative measures from histological sections is both labour intensive and open to interpretation. Contemporary imaging technologies such as optical coherence tomography (OCT) which are now used extensively in both clinical and laboratory practice, have revolutionised the assessment of animal models of retinal disease and circumvent many of the problems associated with traditional histology as presented above (Fischer et al., 2009). In spite of these advances, it has still proved challenging to objectively map broad patterns of outer retinal degeneration *in vivo* which would be of great benefit in the longitudinal assessment of interventions

in animal models of RP. Manual segmentation of OCT images is time-consuming and subject to inter-observer variability and the development of reliable automated systems is a current area of active investigation (Yang et al., 2011). Further, segmentation algorithms built into current OCT software systems fail to accurately and consistently delineate the outer nuclear layer (ONL) in rodents, particularly in degenerative states or following intervention where retinal architecture may be grossly abnormal.

Here we describe a technique which permits the immediate *en face* visualisation of the layer of surviving photoreceptors in mouse models of RP using confocal scanning laser ophthalmoscopy (cSLO). This non-invasive technology uses near infra-red reflectance (NIR) and blue laser sources to stimulate autofluorescent elements within the retina and is used extensively in clinical practice for the diagnosis and assessment of a multitude of ophthalmic disorders (von Rückmann et al., 1995; Wollstein et al., 1998). By crossing a mouse strain that expresses enhanced green fluorescent protein (EGFP) under the control of the rod-specific neural retina-specific leucine zipper (*Nrl)* promoter (Akimoto et al., 2006) with mouse models of RP, we have generated novel strains in which the ONL may be directly visualised using blue autofluorescence (BAF) cSLO imaging. We validate this approach for two widely-used mouse models of RP: the rhodopsin knock-out mouse (Humphries et al., 1997) and the P23H knock-in mouse model of autosomal dominant RP (Sakami et al., 2011), and demonstrate how this technique may allow for the visualisation and quantification of broad spatiotemporal patterns of outer retinal degeneration *in vivo*.

2. Materials & Methods

2.1 Animals

All procedures were performed following approval by the Oxford Animal Ethics Committee in accordance with the UK Home Office Guidelines on the Animal (Scientific Procedures) Act, 1986 and with the Association for Research in Vision & Ophthalmology (ARVO) statements on the care and use

of animals in ophthalmic research. Mice were housed within individually ventilated cages in a 12-hour light-dark cycle environment with food and water available *ad libitum*. The progeny of Tg(*Nrl-EGFP*) mice (kind gift of Anand Swaroop, National Eye Institute, Bethseda, MD; henceforth referred to as *Nrl-EGFP, Rho*$^{+/+}$) and rhodopsin null mice (kind gift of G. Jane Farrar, Dublin) were crossed to generate mice homozygous for the null rhodopsin mutation but carrying the *Nrl-EGFP* allele (henceforth known as *Nrl-EGFP, Rho*$^{-/-}$). Tg(*Nrl-EGFP*) animals were also mated with B6.129S6(Cg)-Rho$^{tm1.1Kpal}$/J mice (Jackson Laboratories, USA) to generate litters heterozygous for both the *Nrl-EGFP* and mutant *Rho*^{P23H} alleles (henceforth referred to as *Nrl-EGFP, Rho*$^{P23H/+}$).

2.2 Retinal Imaging

Mice were anaesthetised by intraperitoneal administration of ketamine (Vetalar, Boehringer Ingelheim, Germany; 80 µg/g body weight) and xylazine (Rompun; Bayer, Germany; 10 µg/g body weight) diluted in sterile 0.9% saline solution. Reversal of anaesthesia was achieved where required by intraperitoneal injection of atipamezole (Antisedan, Zoetis, USA; 2mg/kg body weight) diluted in sterile 0.9% saline solution. Pupils were dilated using tropicamide 1% and phenylephrine hydrochloride 2.5% eye drops (both Bausch & Lomb, Kingston upon Thames, UK). All retinal imaging was performed using the Spectralis ophthalmic imaging platform (Heidelberg Engineering, Germany) with a 55° camera lens. Hypromellose 0.3% drops (Blumont Healthcare Ltd., UK) were instilled bilaterally and polymethyl methacrylate contact lenses of specification 3.2mm diameter, 1.7mm back optic zone radius, 0.4mm central thickness and plano refractive power (Cantor & Nissel Ltd., Brackley, UK), were applied to both eyes and centred over the dilated pupils. The contact lenses served to create a uniform refractive surface for imaging, as well as acting to prevent corneal dehydration, which would otherwise result in the formation of reversible cataract (Charbel Issa et al., 2012). All images were acquired in 'High Resolution' mode (8bits/pixel and 1536 x 1536 pixel resolution) using automatic real-time (ART) functionality. In ART mode, multiple images are acquired and averaged to create a composite with increased resolution. The eye is actively tracked during this process based on high

contrast landmarks, thus compensating for small movements of the eye such as those that occur as a result of respiration. In all cases, a reference image was first taken of the external aspect of the eye using the NIR mode (which utilizes an 815nm wavelength diode laser), before the laser arm was moved forwards and the image focussed on the retina with the optic nerve positioned at the centre of the field of view. The dioptric focus was adjusted to the confocal plane corresponding to that of highest NIR reflectance which is thought to be that of the retinal pigment epithelium (RPE) (Fischer et al., 2009), and the sensitivity set to give the brightest image possible whilst avoiding areas of overexposure. An NIR reflectance image was captured as an average of five or more stills taken in ART mode. BAF cSLO images were subsequently acquired using the inbuilt module of the Spectralis platform. This consisted of a 486nm blue diode excitation laser coupled with a 500nm barrier filter. Emission was recorded between 500nm and 700nm. All fluorescence fundal images were captured at the same focal plane as that used for NIR reflectance image acquisition. BAF images of retinas expressing EGFP were acquired at sensitivity values (a parameter that can be adjusted between values of 31 and 107) of 50, 60 and 70 in ART mode (minimum five frames) with normalisation switched off to allow for subsequent quantification of the fluorescence signal. For semiquantitative analysis of fluorescence from the generated BAF images, a detector sensitivity was selected which gave the highest observed signal without significant areas of saturation. Surface plots were generated from BAF images using the Interactive 3D Surface Plot plugin in ImageJ software (Version 1.50c4; National Institute of Health, USA).

For OCT imaging, the mouse remained in the same position on the viewing platform with the contact lens in situ. The imaging protocol consisted of eight equally spaced radially orientated scans centred on the optic disc. Each image was captured from an average of 25 individual B-scans.

Mean grey value (mGV), which quantifies average signal in a pre-specified area of a greyscale image (Charbel Issa et al., 2012), was calculated from autofluorescence micrographs using ImageJ software.

A region of interest band centred on the optic nerve head with an inner radius of 600 pixels and a width of 255 pixels was used in all cases (Figure 1).

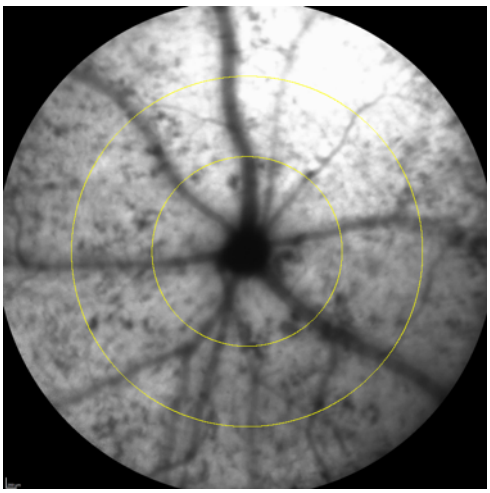

Figure 1. Measurement of mean grey value (mGV) from blue autofluorescence (BAF) cSLO fundus images. All images were centred on the optic disc. ImageJ software was used to create a sampling band (shown in yellow) with inner radius 600 pixels and width 255 pixels centred on the optic disc from which mGV was calculated. The mGV thus quantifies the average signal within the area between the two yellow rings.

2.3 Subretinal Injection

To determine the effects of local insult to photoreceptors on regional fluorescence in the *Nrl-EGFP, Rho*$^{P23H/+}$ model, animals aged post-natal week (PNW) 3 were subjected to single superior subretinal injection of an adeno-associated viral (AAV) vector which in a parallel study was found to be toxic to photoreceptors (n=7). The vector in question was an AAV serotype 2 pseudotyped within the AAV8^{Y733F} capsid expressing the human rhodopsin protein under the control of a human rhosopsin-CAG hybrid promoter with a 3' woodchuck hepatitis virus post-transcriptional regulatory element (WPRE) and a bovine growth hormone polyA signal (AAV2/8^{Y733F}.hRHOp-CAG.RHO.WPRE.pA). Animals were anaesthetised and the pupils dilated as described above. Prior to injection, a drop of proxymetacaine

(Minims, Bausch & Lomb, Kingston upon Thames, UK) was applied to provide additional topical anaesthesia. The animal was positioned on a customised foam operating mat beneath a foot pedal controlled microsurgical operating microscope. A paracentesis was performed by brief puncture of the mid-peripheral corneal with a 33G needle. This induced the efflux of a small bleb of aqueous after which the wound self-sealed. Carbomer gel (Viscotears Liquid Gel, Alcon, Camberley, UK) was then applied liberally to the corneal surface and a 5mm glass coverslip rested on top. This allowed direct visualization of the posterior pole through the operating microscope. A 35G bevelled NanoFil needle was mounted on a Nanofil 10µl syringe (both World Precision Instruments, Hitchin, UK) and 2 x 10^9 genome copies of the AAV vector in 1.5µl of phosphate-buffered saline (PBS; ThermoFisher Scientific, Milton Keynes, UK) was drawn up in preparation for injection. The superior rectus muscle was grasped with notched forceps to stabilize the eye and the needle was carefully introduced through the adjacent sclera and into the subretinal space under direct visualisation. Once the entirety of the needle's bevel was visible beneath the retina, the superior rectus muscle was released and the syringe plunger depressed creating a bullous superior hemi-retinal detachment. The needle was then carefully withdrawn, the glass cover slip removed, and a chloramphenicol drop (Minims, Bausch & Lomb, Kingston upon Thames, UK) instilled.

2.4 Histology

In preparation for histological analysis, the cornea, iris and lens were removed from enucleated eyes. The resulting eye cups were fixed in 4% paraformaldehyde for 30 minutes then cryopreserved sequentially in a 10-30% sucrose gradient. Specimens were subsequently embedded within optimal cutting temperature compound (VWR, Lutterworth, UK), frozen on dry ice and sectioned to a thickness of 18µm. Slides were counterstained with Hoescht 33342 (1:4,000), mounted with Prolong Diamond antifade media (ThermoFisher Scientific, Milton Keynes, UK) and imaged by confocal microscopy using the LSM-710 inverted confocal microscope system (Zeiss, Oberkochen, Germany).

3 Results

3.1 Natural history of fluorescence decay in the Nrl-EGFP, Rho$^{-/-}$ retina

To validate the use of cSLO as a tool to directly observe and track the progressive loss of rods in degenerate *Nrl-EGFP* models, longitudinal imaging along with histology was performed first in the *Nrl-EGFP, Rho$^{-/-}$* mouse (Figure 2). The distribution of observed fluorescence in these retinas did not suggest any gross regional differences in the extent of photoreceptor loss at any observational time point (Figure 2A). At PNW3, the mGV measured from BAF images was reduced to 35% of that recorded from age-matched *Nrl-EGFP, Rho$^{+/+}$* retinas at a detector sensitivity of 60. Over the following nine weeks, mGV measured decreased rapidly in the *Nrl-EGFP, Rho$^{-/-}$* model (Figure 2B). Mean mGV recorded from *Nrl-EGFP, Rho$^{+/+}$* eyes initially increased between PNW3 and PNW6 and then showed a very slight decline up to the last time point recorded at PNW15 (Figure 2B). The difference in mGV between the two models was highly significant ($F(1.7, 30.4)=5.79$, $p=0.01$ for effect of time; $F(1, 18)=649.9$, $p<0.0001$ for effect of model, $F(4, 72)=13.22$, $p<0.0001$ for interaction model x time, repeated measures two-way ANOVA). Fluorescence microscopy of histological sections over this time period demonstrated progressive thinning of the green fluorescent ONL in the *Nrl-EGFP, Rho$^{-/-}$*, but not in the *Nrl-EGFP, Rho$^{+/+}$* retina (Figure 2C).

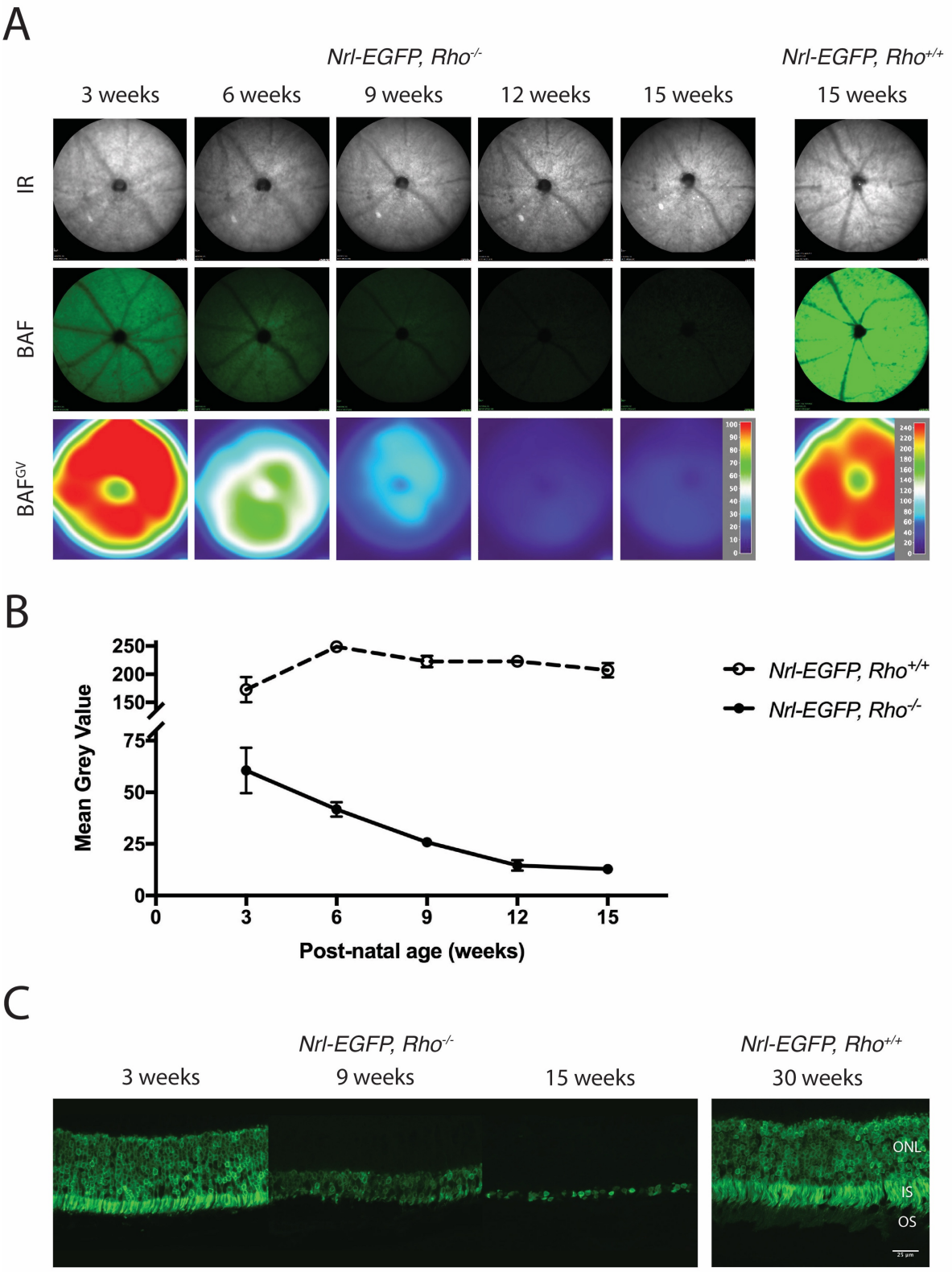

210

211 **Figure 2. Natural history of fluorescence decay in the *Nrl-EGFP, Rho*$^{-/-}$ mouse retina. (A)** Longitudinal

212 confocal cSLO imaging of a representative animal between postnatal weeks 3 and 15. Upper panels

show near infrared (IR) images. Middle panels show blue autofluorescence (BAF) micrographs captured in the same focal plane as their corresponding IR images, acquired at a detector sensitivity of 60. Lower panels show corresponding surface plots in which grey value for each pixel within BAF images has been colour coded according to the inset scale (BAF^{GV}). Note that different scales have been applied for *Nrl-EGFP, Rho*$^{-/-}$ and *Nrl-EGFP, Rho*$^{+/+}$ models so that spatial patterns within individual surface plots might be better appreciated. **(B)** Mean grey value +/- standard error of the mean (SEM) as a function of time recorded from BAF images at a sensitivity of 60 for *Nrl-EGFP, Rho*$^{-/-}$ eyes (n=12) and *Nrl-EGFP, Rho*$^{+/+}$ eyes (n=8). For points where no error bar is displayed, the SEM is smaller than the size of the symbol. **(C)** Fluorescence microscopy of retinal cryosections derived from *Nrl-EGFP, Rho*$^{-/-}$ mice at PNW 3, 9 and 15, and from an *Nrl-EGFP, Rho*$^{+/+}$ mouse at PNW30. ONL: outer nuclear layer; IS: inner segments; OS: outer segments.

3.2 Natural history of fluorescence decay in the Nrl-EGFP, Rho$^{P23H/+}$ retina

The same imaging protocol was next applied to *Nrl-EGFP, Rho*$^{P23H/+}$ mice. At PNW3, mGV was 41.6% of that recorded in *Nrl-EGFP, Rho*$^{+/+}$ mice at a detector sensitivity of 60. The mGV steadily decreased over time in the *Nrl-EGFP, Rho*$^{P23H/+}$ model ($F(5, 90)=17.9$, $p<0.0001$ for effect of time, repeated measures two-way ANOVA), but at a rate slower than that observed in the knockout eye (Figure 3). As previously described in the *Rho*$^{P23H/+}$ knock-in mouse (Sakami et al., 2014), degeneration in the *Nrl-EGFP, Rho*$^{P23H/+}$ retina was markedly faster in the inferior than in the superior retina (Figure 3). This difference was detectable *in vivo* by cSLO BAF imaging (Figure 3A). Histological examination of these retinas revealed shortened IS and rudimentary or absent OS when compared with the *Rho*$^{+/+}$ model (Figure 3C).

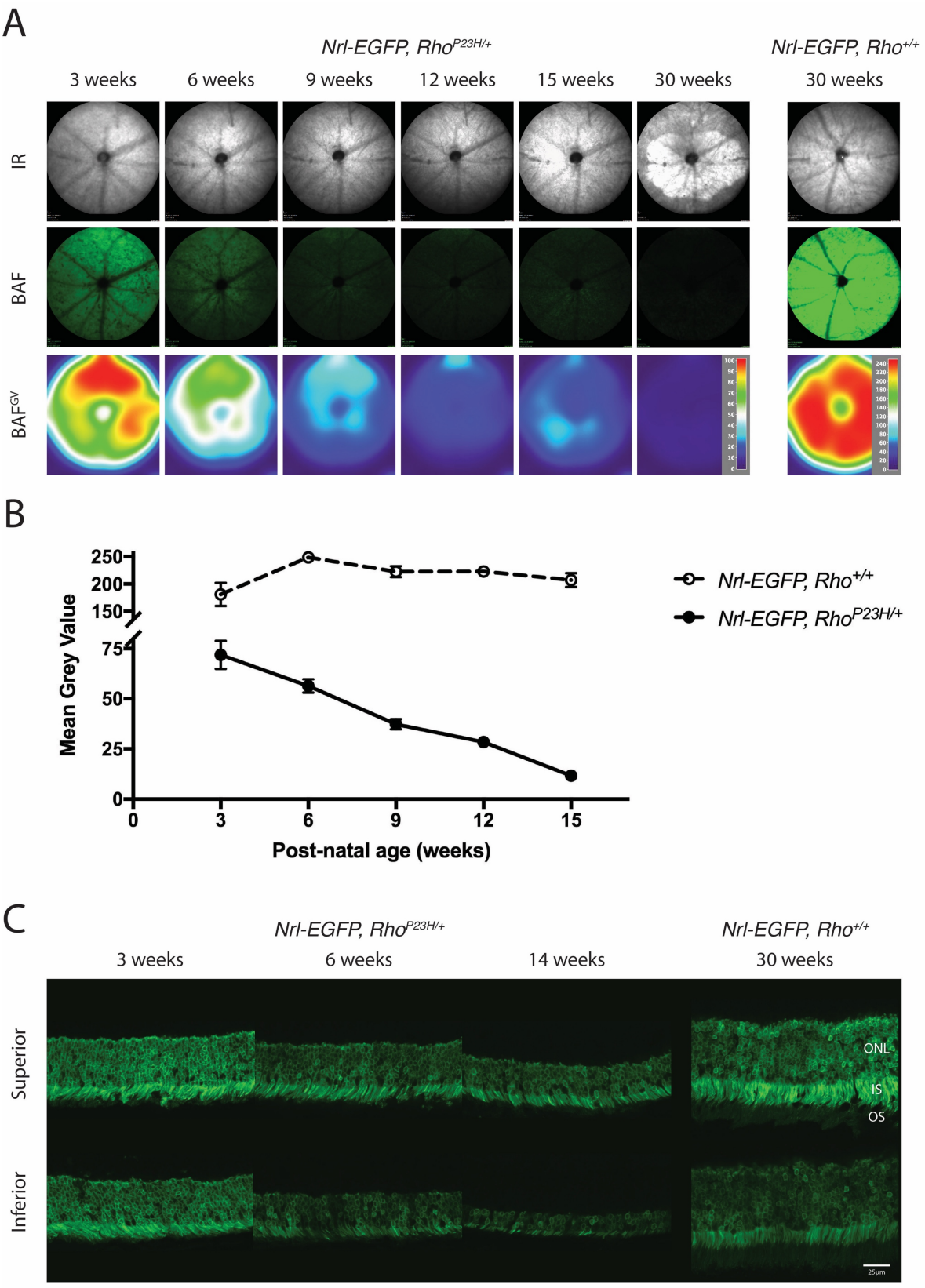

236

237 **Figure 3. Natural history of fluorescence decay in the *Nrl-EGFP, Rho$^{P23H/+}$* mouse retina. (A)**

238 Longitudinal confocal cSLO imaging of a representative animal between postnatal weeks 3 and 30.

Upper panels show near infrared (IR) images. Middle panels show blue autofluorescence (BAF) micrographs captured in the same focal plane as their corresponding IR images, acquired at a detector sensitivity of 60. Lower panels show corresponding surface plots in which grey value for each pixel within BAF images has been colour coded according to the inset scale (BAF^{GV}). Note that different scales have been applied for *Nrl-EGFP, Rho*$^{P23H/+}$ and *Nrl-EGFP, Rho*$^{+/+}$ models so that spatial patterns within individual surface plots might be better appreciated. **(B)** Mean grey value +/- SEM as a function of time recorded from BAF images at a sensitivity of 60 for *Nrl-EGFP, Rho*$^{P23H/+}$ eyes (n=12) and *Nrl-EGFP, Rho*$^{+/+}$ (n=8) eyes. For points where no error bar is displayed, the SEM is smaller than the size of the symbol. **(C)** Fluorescence microscopy of retinal cryosections derived from *Nrl-EGFP, Rho*$^{P23H/+}$ mice at PNW 3, 6 and 14, and from an *Nrl-EGFP, Rho*$^{+/+}$ mouse at PNW30. Images were acquired of the midperipheral retina from vertically orientated cryosections in the plane of the optic disc at equal distances superior and inferior of the nerve head margin. Note the more rapid thinning of the green fluorescent ONL in the inferior than the superior retina in the *Nrl-EGFP, Rho*$^{P23H/+}$ model. ONL: outer nuclear layer; IS: inner segments; OS: outer segments.

3.3 Regional differences in outer retinal degeneration may be detected by mGV calculation

Mean grey values were calculated from superior and inferior hemi-retinal images of mice aged PNW9 of all three genotypes: *Nrl-EGFP, Rho*$^{+/+}$ (n=8), *Nrl-EGFP, Rho*$^{-/-}$ (n=12), *Nrl-EGFP, Rho*$^{P23H/+}$ (n=15). Whilst no significant difference in mGV was detected between superior and inferior retinal hemispheres for *Nrl-EGFP, Rho*$^{+/+}$ and *Nrl-EGFP, Rho*$^{-/-}$ mice ($p=0.37$ and $p=0.89$ respectively), the mGV of the superior retinal hemisphere was significantly greater than that of the inferior hemisphere in the *Nrl-EGFP, Rho*$^{P23H/+}$ model ($p<0.0001$, t-tests with Holm-Sidak's correction for multiple comparisons).

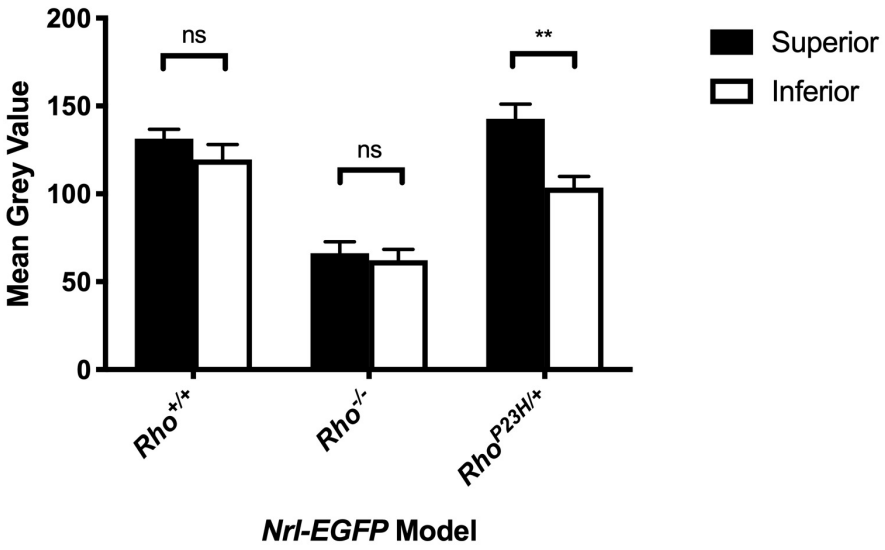

Figure 4. Mean grey values +/- SEM for the superior and inferior retinal hemispheres in *Nrl-EGFP* models. Measurements were taken from BAF hemi-retinal images of mice aged PNW9 for *Nrl-EGFP, Rho$^{+/+}$*, *Nrl-EGFP, Rho$^{-/-}$* and *Nrl-EGFP, Rho$^{P23H/+}$* mice at detector sensitivities of 50, 70 and 70 respectively. A lower acquisition sensitivity was selected for the *Nrl-EGFP, Rho$^{+/+}$* model to avoid image saturation and allow all three to be displayed on a single scale. ns: not significant, **p<0.001.

3.4 cSLO may detect focal loss of photoreceptor in vivo

As part of a parallel study, *Nrl-EGFP, Rho$^{P23H/+}$* mice aged PNW3 received single superior subretinal injections of an AAV vector at a dose which was found to be toxic to photoreceptors. Four weeks later, cSLO and OCT imaging was performed. Figure 5 shows images acquired from a representative mouse. A reduction in overall green fluorescence was apparent in the superior hemiretina of injected eyes when compared to fellow uninjected eyes (Figure 5B and C). This reduction in fluorescence was associated with a stippled appearance in this region on IR imaging (Figure 5A). Areas of absence of fluorescence corresponded to regions of near-complete ONL wipe-out as seen by OCT (Figure 5, C and D). Confocal fluorescence imaging may thus be used to map focal areas of photoreceptor loss following local insult in *Nrl-EGFP* mouse models.

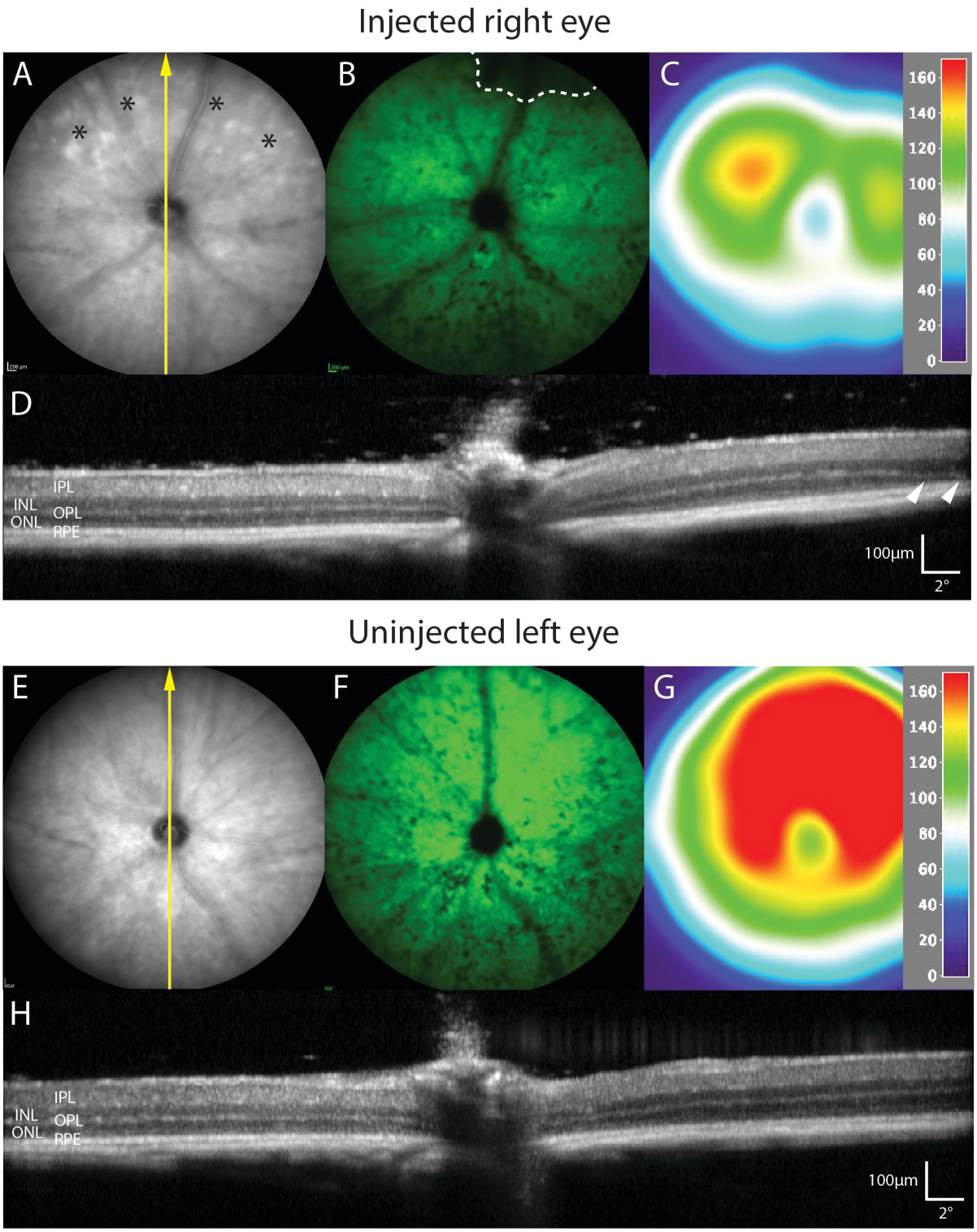

Figure 5. Regional loss of rod photoreceptors may be mapped in an *Nrl-EGFP* model of RP following subretinal injection of AAV. Images of *Nrl-EGFP, Rho*$^{P23H/+}$ retinas were captured using NIR (A & E), BAF (B & F) and OCT (D & H) imaging modalities four weeks after injection of an AAV vector at a dose that was found to be toxic to rods. Panels C and G show BAF^{GV} surface plots derived from the BAF

images in panels B and F respectively. The orientation of each OCT scan is indicated by a yellow arrow in the corresponding NIR image. A stippled appearance in the superior hemi-retina (indicated by asterisks) could be appreciated on NIR imaging of the injected eye (A), which was not present on the uninjected side (E). This was associated with a relative reduction in observed green fluorescence in the superior hemiretina of injected versus uninjected eyes (B and C versus F & G). An area of near complete absence of fluorescence can be appreciated close to the injection site on BAF imaging (dotted line in B). This corresponded to a region of severe ONL thinning observed on OCT imaging (white arrowheads in D). IPL: inner plexiform layer; OPL: outer plexiform layer; INL: inner nuclear layer; ONL: outer nuclear layer; RPE: retinal pigment epithelium.

4 Discussion

Here we have developed and validated two novel *Nrl-EGFP* transgenic mouse models of rhodopsin-related RP: *Nrl-EGFP*, $Rho^{-/-}$ and *Nrl-EGFP*, $Rho^{P23H/+}$. These mice have rods that are labelled with EGFP permitting their direct visualization *in vivo* using *en face* BAF cSLO imaging. This provides a simple and convenient means of tracking the loss of rods longitudinally in any given animal over time, and allows broad spatial patterns of degeneration to be readily determined. Use of Nrl-EGFP mouse models also allows the extent of focal loss of photoreceptors to be objectively mapped *en face* after a photoreceptor-specific toxic insult. It follows that any rescue effect associated with an experimental intervention should be similarly discernible.

Blue autofluorescence imaging is well established in the initial diagnosis and subsequent monitoring of both inherited and acquired retinal disease in the clinical setting (Schmitz-Valckenberg et al., 2008). RPE-derived lipofuscin is the predominant fluorophore responsible for this signal (Delori et al., 1995; Sparrow and Boulton, 2005). Hypo-autofluorescence may thus indicate RPE loss as occurs centrally in

geographic atrophy associated with advanced age-related macular degeneration (AMD) (Holz et al., 2001), or peripherally in IRDs such or choroideremia (Xue et al., 2016). Peripheral hypo-autofluorescence is frequently observed in RP owing to reduced metabolic demand on the RPE as a result of overlying photoreceptor loss (von Rückmann et al., 1999). Hyper-autofluorescence may indicate areas of RPE dysfunction for example in the case of hyper-autofluorescent rings that are commonly seen at the leading edge of degeneration in RP (Jolly et al., 2016; Robson et al., 2006), or as a result of abnormal lipofuscin accumulation as occurs in AMD and *ABCA4*-related maculopathy (Stargardt disease) (Sparrow and Boulton, 2005). Quantitative autofluorescence (qAF) using mean grey levels in a similar fashion to this study has also been applied to aid in diagnosis and track progression in patients with IRDs (Sparrow et al., 2019). This technique has been adapted for use in mouse models of IRDs to quantify the build-up of autofluorescent deposits (primarily the bisretinoid A2E) within the RPE (Charbel Issa et al., 2013), and has been used as a tool to demonstrate efficacy of both deuterated vitamin A (Charbel Issa et al., 2015) and an AAV-mediated gene therapy (McClements et al., 2018) in the *Abca4*$^{-/-}$ mouse model of Stargardt disease.

There are a number of limitations associated with the application of BAF imaging to the spatiotemporal assessment of rod degeneration in *Nrl-EGFP* models of retinal disease. Firstly, the approach would need to be individually validated for each species and mutation prior to experimental application. Further, it assumes the availability of a cSLO platform for image acquisition. Secondly, the widespread expression of EGFP in models of RP has the potential to mask the signal from other retinal fluorophores that may accumulate in such animals. Indeed, hyperfluorescent spots which are thought to represent lipofuscin-laden subretinal macrophages (Luhmann et al., 2013, 2009) have been noted in several rodent models of RP, including *Rho*$^{-/-}$ (Huber et al., 2009), when imaging by cSLO in BAF mode. Although these spots were not generally discernible from background EGFP signal in either the *Nrl-EGFP, Rho*$^{-/-}$ or *Nrl-EGFP, Rho*$^{P23H/+}$ retina, such autofluorescent elements might explain the areas of increased signal sometimes observed at week 15 (see Figure 3A) . Secondly, the BAF signal recorded

from these models may be influenced by a number of other factors aside from ONL thickness including pupil size, media opacity such as cataract or vitreous haemorrhage, contact lens centration and variation in confocal plane (Charbel Issa et al., 2012). Indeed, the observed increase in mGV recorded in the *Nrl-EGFP, Rho*$^{+/+}$ mouse between PNW3 and PNW6 (see Figures 2B & 3B) likely reflects the relatively large commensurate increase in pupillary area that occurs over this time period rather than any change in retinal EGFP expression.

The accuracy of mGV measurements may further be adversely affected if areas of signal saturation occur within an image. This may necessitate the acquisition of multiple BAF images at a range of detector sensitivity settings at each time-point from which the most appropriate may be selected after collection of all data.

These factors may limit the accuracy of mGV as a global representative measure of surviving ONL, and measurements derived from SD-OCT are likely to represent more consistent and clinically relevant metrics. The strength of BAF cSLO imaging in *Nrl-EGFP* models of RP lies in the generation of the images themselves, which represent qualitative *en face* maps of regional rod survival that do not rely on processing or analysis following image acquisition.

Finally, it is possible that the expression of EGFP within rods may have an impact on the natural history of photoreceptor loss in degenerate models, which would of course detract from their clinical relevance. Although no degeneration was observed in the *Nrl-EGFP, Rho*$^{+/+}$ mouse, the possibility of such an interaction cannot be excluded.

In summary, the use of novel *Nrl-EGFP* models of retinitis pigmentosa in combination with serial cSLO BAF imaging can permit non-invasive spatiotemporal mapping of rod cell degeneration *in vivo*. This

technique may prove useful in the pre-clinical evaluation of novel therapeutics for the treatment of retinitis pigmentosa.

References

Akimoto, M., Cheng, H., Zhu, D., Brzezinski, J.A., Khanna, R., Filippova, E., Oh, E.C.T., Jing, Y., Linares, J.-L., Brooks, M., Zareparsi, S., Mears, A.J., Hero, A., Glaser, T., Swaroop, A., 2006. Targeting of GFP to newborn rods by Nrl promoter and temporal expression profiling of flow-sorted photoreceptors. Proc. Natl. Acad. Sci. 103, 3890–3895. https://doi.org/10.1073/pnas.0508214103

Charbel Issa, P., Barnard, A.R., Herrmann, P., Washington, I., MacLaren, R.E., 2015. Rescue of the Stargardt phenotype in Abca4 knockout mice through inhibition of vitamin A dimerization. Proc. Natl. Acad. Sci. 112, 8415 LP – 8420.

Charbel Issa, P., Barnard, A.R., Singh, M.S., Carter, E., Jiang, Z., Radu, R.A., Schraermeyer, U., MacLaren, R.E., 2013. Fundus Autofluorescence in the Abca4−/− Mouse Model of Stargardt Disease—Correlation With Accumulation of A2E, Retinal Function, and HistologyFundus Autofluorescence in the Abca4 −/− Mouse. Invest. Ophthalmol. Vis. Sci. 54, 5602–5612. https://doi.org/10.1167/iovs.13-11688

Charbel Issa, P., Singh, M.S., Lipinski, D.M., Chong, N. V., Delori, F.C., Barnard, A.R., MacLaren, R.E., 2012. Optimization of in vivo confocal autofluorescence imaging of the ocular fundus in mice and its application to models of human retinal degeneration. Investig. Ophthalmol. Vis. Sci. 53, 1066–1075. https://doi.org/10.1167/iovs.11-8767

Delori, F.C., Dorey, C.K., Staurenghi, G., Arend, O., Goger, D.G., Weiter, J.J., 1995. In vivo fluorescence of the ocular fundus exhibits retinal pigment epithelium lipofuscin characteristics. Invest. Ophthalmol. Vis. Sci. 36, 718–729.

Fischer, M.D., Huber, G., Beck, S.C., Tanimoto, N., Muehlfriedel, R., Fahl, E., Grimm, C., Wenzel, A., Remé, C.E., van de Pavert, S.A., Wijnholds, J., Pacal, M., Bremner, R., Seeliger, M.W., 2009.

Noninvasive, in vivo assessment of mouse retinal structure using optical coherence tomography. PLoS One 4. https://doi.org/10.1371/journal.pone.0007507

Hartong, D.T., Berson, E.L., Dryja, T.P., 2006. Retinitis pigmentosa. Lancet 368, 1795–809.

Holz, F.G., Bellman, C., Staudt, S., Schütt, F., Völcker, H.E., 2001. Fundus Autofluorescence and Development of Geographic Atrophy in Age-Related Macular Degeneration. Invest. Ophthalmol. Vis. Sci. 42, 1051–1056.

Huber, G., Beck, S.C., Grimm, C., Sahaboglu-Tekgoz, A., Paquet-Durand, F., Wenzel, A., Humphries, P., Redmond, T.M., Seeliger, M.W., Fischer, M.D., 2009. Spectral Domain Optical Coherence Tomography in Mouse Models of Retinal Degeneration. Investig. Opthalmology Vis. Sci. 50, 5888. https://doi.org/10.1167/iovs.09-3724

Humphries, M.M., Rancourt, D., Farrar, G.J., Kenna, P.F., Hazel, M., Bush, R.A., Sieving, P.A., Sheils, D.M., McNally, N., Creighton, P., Erven, A., Boros, A., Gulya, K., Capecchi, M.R., Humphries, P., 1997. Retinopathy induced in mice by targeted disruption of the rhodopsin gene. Nat. Genet. 15, 57–61.

Jolly, J.K., Wagner, S.K., Moules, J., Gekeler, F., Webster, A.R., Downes, S.M., MacLaren, R.E., 2016. A Novel Method for Quantitative Serial Autofluorescence Analysis in Retinitis Pigmentosa Using Image Characteristics. Transl. Vis. Sci. Technol. 5, 10. https://doi.org/10.1167/tvst.5.6.10

Luhmann, U.F.O., Carvalho, L.S., Robbie, S.J., Cowing, J.A., Duran, Y., Munro, P.M.G., Bainbridge, J.W.B., Ali, R.R., 2013. Ccl2, Cx3cr1 and Ccl2/Cx3cr1 chemokine deficiencies are not sufficient to cause age-related retinal degeneration. Exp. Eye Res. 107, 80–87. https://doi.org/https://doi.org/10.1016/j.exer.2012.11.015

Luhmann, U.F.O., Robbie, S., Munro, P.M.G., Barker, S.E., Duran, Y., Luong, V., Fitzke, F.W., Bainbridge, J.W.B., Ali, R.R., MacLaren, R.E., 2009. The Drusenlike Phenotype in Aging Ccl2-Knockout Mice Is Caused by an Accelerated Accumulation of Swollen Autofluorescent Subretinal Macrophages. Invest. Ophthalmol. Vis. Sci. 50, 5934–5943. https://doi.org/10.1167/iovs.09-3462

McClements, M.E., Barnard, A.R., Singh, M.S., Charbel Issa, P., Jiang, Z., Radu, R.A., MacLaren, R.E., 2018. An AAV Dual Vector Strategy Ameliorates the Stargardt Phenotype in Adult Abca4−/− Mice. Hum. Gene Ther. 30, 590–600. https://doi.org/10.1089/hum.2018.156

McInnes, E., 2005. Artefacts in histopathology. Comp. Clin. Path. 13, 100–108. https://doi.org/10.1007/s00580-004-0532-4

Rivas, M. a, Vecino, E., 2009. Animal models and different therapies for treatment of retinitis pigmentosa. Histol Histopathol 24, 1295–1322. https://doi.org/10.14670/HH-24.1295

Robson, A.G., Saihan, Z., Jenkins, S.A., Fitzke, F.W., Bird, A.C., Webster, A.R., Holder, G.E., 2006. Functional characterisation and serial imaging of abnormal fundus autofluorescence in patients with retinitis pigmentosa and normal visual acuity. Br. J. Ophthalmol. 90, 472 LP – 479. https://doi.org/10.1136/bjo.2005.082487

Sakami, S., Kolesnikov, A. V., Kefalov, V.J., Palczewski, K., 2014. P23H opsin knock-in mice reveal a novel step in retinal rod disc morphogenesis. Hum. Mol. Genet. 23, 1723–1741. https://doi.org/10.1093/hmg/ddt561

Sakami, S., Maeda, T., Bereta, G., Okano, K., Golczak, M., Sumaroka, A., Roman, A.J., Cideciyan, A. V., Jacobson, S.G., Palczewski, K., 2011. Probing mechanisms of photoreceptor degeneration in a new mouse model of the common form of autosomal dominant retinitis pigmentosa due to P23H opsin mutations. J. Biol. Chem. 286, 10551–10567. https://doi.org/10.1074/jbc.M110.209759

Schmitz-Valckenberg, S., Holz, F.G., Bird, A.C., Spaide, R.F., 2008. Fundus Autofluorescence Imaging: Review and Perspectives. Retina 28.

Smith, J., Ward, D., Michaelides, M., Moore, A.T., Simpson, S., 2015. New and emerging technologies for the treatment of inherited retinal diseases: a horizon scanning review. Eye 29, 1131–1140. https://doi.org/10.1038/eye.2015.115

Sparrow, J.R., Boulton, M., 2005. RPE lipofuscin and its role in retinal pathobiology. Exp. Eye Res. 80, 595–606. https://doi.org/https://doi.org/10.1016/j.exer.2005.01.007

Sparrow, J.R., Duncker, T., Schuerch, K., Paavo, M., Ronaldo, J., Carvalho, L. De, 2019. Lessons learned from quantitative fundus autofluorescence. Prog. Retin. Eye Res. https://doi.org/10.1016/j.preteyeres.2019.100774

von Rückmann, a, Fitzke, F.W., Bird, a C., 1995. Distribution of fundus autofluorescence with a scanning laser ophthalmoscope. Br. J. Ophthalmol. 79, 407–12. https://doi.org/10.1136/bjo.79.5.407

von Rückmann, A., Fitzke, F.W., Bird, A.C., 1999. Distribution of pigment epithelium autofluorescence in retinal disease state recorded in vivo and its change over time. Graefe's Arch. Clin. Exp. Ophthalmol. 237, 1–9. https://doi.org/10.1007/s004170050186

Wollstein, G., Garway-Heath, D.F., Hitchings, R.A., 1998. Identification of early glaucoma cases with the scanning laser ophthalmoscope. Ophthalmology 105, 1557–1563. https://doi.org/10.1016/S0161-6420(98)98047-2

Xue, K., Oldani, M., Jolly, J.K., Edwards, T.L., Groppe, M., Downes, S.M., MacLaren, R.E., 2016. Correlation of Optical Coherence Tomography and Autofluorescence in the Outer Retina and Choroid of Patients With Choroideremia. Invest. Ophthalmol. Vis. Sci. 57, 3674–3684. https://doi.org/10.1167/iovs.15-18364

Yang, Q., Reisman, C. a, Chan, K., Ramachandran, R., Raza, a, Hood, D.C., 2011. Automated segmentation of outer retinal layers in macular OCT images of patients with retinitis pigmentosa. Biomed Opt Express 2, 2493–2503. https://doi.org/10.1364/boe.2.002493